Chemical
Science

EDGE ARTICLE

View Article Online
View Journal | View Issue

Check for updates

Cite this: *Chem. Sci.*, 2021, **12**, 10097

All publication charges for this article have been paid for by the Royal Society of Chemistry

Received 20th April 2021
Accepted 24th June 2021

DOI: 10.1039/d1sc02203b

rsc.li/chemical-science

Precision photothermal therapy and photoacoustic imaging by *in situ* activatable thermoplasmonics†

Yahua Liu,‡ Fengye Mo,‡ Jialing Hu, Qunying Jiang, Xiuyuan Wang, Zhiqiao Zou, Xian-Zheng Zhang, Dai-Wen Pang and Xiaoqing Liu *

Phototherapy holds great promise for disease treatment; however, traditional "always-on" photoagents have been restricted to clinical translation due to their nonspecific response and side effects on normal tissues. Here, we show a tumor microenvironment activated photothermal and photoacoustic agent as an activatable prodrug and probe that allows precise cancer diagnosis and treatment. Such an *in situ* revitalized therapeutic and contrast agent is achieved *via* controllable plasmonic heating for thermoplasmonic activation. This enables monitoring of signal molecule dynamics, real-time photothermal and photoacoustic imaging of tumors and lymph node metastasis, and targeted photothermal therapy without unwanted phototoxicity to normal tissues. Our study provides a practical solution to the non-specificity problem in phototherapy and offers precision cancer therapeutic and theranostic strategies. This work may advance the development of ultrasensitive disease diagnosis and precision medicine.

Introduction

Phototherapy such as photodynamic therapy (PDT) and photothermal therapy (PTT) employs photosensitive chemicals to generate reactive oxygen species (ROS) or heat under light irradiation. Besides acting as phototherapeutic agents, these photo-agents can also serve as imaging probes for allowing both therapeutics and theranostics.[1–4] For example, photothermal agents increase the environmental temperature upon laser irradiation, generating thermoelastic expansion and acoustic waves, which can be converted to photoacoustic signals.[5] Such photo-based modality holds great potential for disease treatment or diagnosis due to its noninvasiveness, spatiotemporal selectivity, and negligible drug resistance.[6–11] However, the traditional "always-on" photo-agents including photosensitizers and photothermal chemicals would inevitably provoke a response or phototoxicity to normal tissues,[12–18] and are unable to achieve precise imaging or therapy nor advance the clinical translation of the photoagents.[19–21]

The design of activatable photo-agents offers an innovative approach to nonspecific responses.[22–28] *In situ* activating phototherapy agents in tumor sites will precisely and effectively suppress cancer without side effects. Despite the very recent advances in designing "turn-on" phototherapy agents, practical methods to directly activate cancer phototherapy from pre-existing dormant photo-agents remain elusive, which may offer abundant revived agents for precise and accurate targeted treatments.[21] To date, some organic photosensitizers have been synthesized which could switch photodynamic therapy from "off" to "on" upon stimuli;[25] however, these photosensitizers are neither simple to prepare nor resistant to photobleaching. Another relevant recent example described photothermal agents that were later produced *via* a reaction between the precursor and specific signal molecules in tumors.[29,30] Yet, the *in vivo* yield or efficacy of the later produced agent in such a method is more prone to be constrained by the signal molecule level in the tumor microenvironment and the agent type.

Here, we demonstrate an activatable photoagent as a prodrug and probe for precision cancer treatment and diagnosis by *in situ* revitalization of pre-existing dormant photothermal chemicals (Scheme 1). Plasmonic nanoarchitectures are tailored as biocompatible photoagents to switch off light-to-heat conversion through hybridization of localized surface plasmon resonance (LSPR). Sequential tumor targeted accumulation and tumor environment activation reenergize the pre-synthesized dormant nanoparticles for plasmonic heating because the overexpressed H_2O_2 in the tumor environment triggers notable red-shifted LSPR and recovers the light-to-heat conversion. The photothermal prodrug is thus efficiently *in situ* activated for controllable thermoplasmonics, exhibiting superior photothermal conversion efficiency (49%) over reported agents,[31–34] and strong photoacoustic and fluorescence signals. As a result, this approach not only achieves precision photothermal treatment without side effects on normal tissues, but

---

College of Chemistry and Molecular Sciences, Wuhan University, Wuhan 430072, P. R. China. E-mail: xiaoqingliu@whu.edu.cn

† Electronic supplementary information (ESI) available: Experimental details; synthesis and characterization; additional *in vitro* and *in vivo* analysis. See DOI: 10.1039/d1sc02203b

‡ These authors contributed equally to this work.

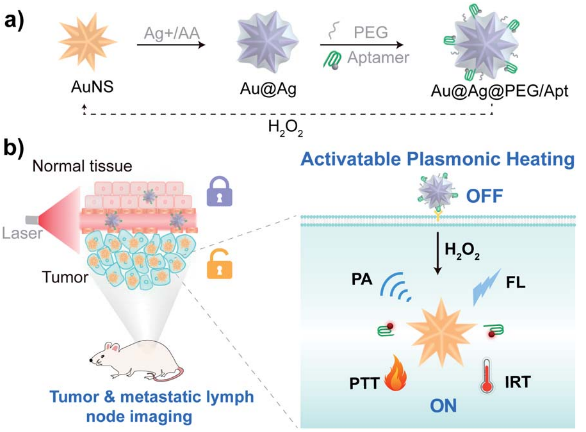

Scheme 1 Illustration of precise cancer therapeutic and theranostic approaches with an *in situ* activated photothermal and photoacoustic agent as a prodrug and probe to specifically eradicate cancer cells and sensitively image primary and metastatic tumors. (a) Preparation of plasmonic nanoparticles with tumor microenvironment-tuned LSPR as a prodrug of photoagent for activatable thermoplasmonics. (b) *In situ* activation of the dormant photoagent by microenvironment cues enables sensitive detection of signal molecules, precise imaging of tumors and metastatic lymph nodes, and cancer targeted and activated photothermal therapy (PTT). Briefly, after targeting tumor tissues *via* the specific recognition of nucleolin overexpressed on the surface of cancer cells by aptamers, the dormant nanoagent is reenergized to induce strong LSPR absorption in the NIR range, due to the etching of the plasmonic nanostructure with overexpressed H_2O_2. This allows revitalizing light-to-heat conversion, generating fluorescence (FL), photothermal (infrared thermal, IRT) and photoacoustic (PA) signals, and sensitive bioanalysis and monitoring of H_2O_2 dynamics *in vitro* and *in vivo*. As such, this approach achieves precise imaging of tumors and metastatic lymph nodes, and photothermal ablation of tumors with high specificity.

also allows sensitive probing of signal molecule dynamics and precise photothermal and photoacoustic imaging of tumors and lymph node metastasis. To the best of our knowledge, this method represents the first activatable cancer therapeutic and/or theranostic approach through revitalizing thermoplasmonics, offering a practical and applicable photothermal/photoacoustic agent with engineered precision nanoparticles for translational studies.[19–21]

Results and discussion

An activatable photothermal and photoacoustic agent by plasmonic heating modulation

The procedure for the synthesis of plasmonic nanoparticles is presented in Scheme 1a. Monodispersed gold nanostars (AuNS) with an average diameter of around 60 nm were first prepared *via* a seed-mediated growth method (Fig. S1†). Silver-coated gold (Au@Ag) nanostars were subsequently prepared through the reduction of silver ions by ascorbic acid (AA). Upon adding increased amounts of Ag^+ into AuNS solution, the hydrodynamic size of the particles was increased from 63.9 nm to 75.1 nm (Fig. S2†), indicating the formation of Au@Ag nanostars. Moreover, LSPR of the nanostars gradually blue-shifted as more Ag deposited (Fig. 1A) due to the plasmonic hybridization of gold and silver.[35–38] Notable reduced absorption in the NIR region and a blue-shifted plasmon resonance peak were observed when the silver ion concentration was increased from 0 to 0.5 mM (Fig. 1A), suggesting the attenuated photothermal conversion efficiency of gold nanomaterials.[39] Correspondingly, upon irradiation with near-infrared light, there was a stronger inhibition in the temperature elevation of the nanoparticle solution as more Ag^+ reduced to AuNS (Fig. 1B). For the practical application of photothermal agents in cancer therapeutics, we first optimized the synthesis approach to assure efficacy and safety. The heating kinetics showed that the temperature of the Au@Ag nanostars prepared with Ag^+ more than 0.1 mM concentration was below the critical threshold of 43 °C to kill cancer cells.[40] Whereas etching of the silver shell with H_2O_2 (100 μM) restored the marvelous heating capability of the nanostars (Fig. 1C). It should be noted that the concentration of H_2O_2 in the tumor stroma is about 50–100 μM,[41,42] and the above H_2O_2 level is applicable. Specifically, for the Au@Ag nanostars prepared with Ag^+ of less than 0.5 mM concentration, the temperature elevation could be greatly enhanced upon H_2O_2 activation, rising above the temperature tolerance threshold of cancer cells. The switch between the dormant and activated states was illustrated by the statistics of respective temperature profiles (Fig. 1D), and a medium level Ag^+ (0.3 mM) was utilized to prepare Au@Ag nanostars for biomedical studies.

To improve physiological stability and acquire strong tumor targeting capability, PEG and aptamer AS1411 were successively conjugated onto the surface of Au@Ag nanostars through the Ag–S bond to obtain Au@Ag@PEG/Apt nanostars, due to the well-known stealth character of PEG during blood circulation,[43,44] and the specific recognition of overexpression of nucleolin on the cancer cell membrane by the AS1411 aptamer.[45] After PEG and aptamer conjugation, the hydrodynamic size became bigger consecutively, while the maximum absorption peak remained the same (Fig. 1E and F). In addition, Au@Ag@PEG/Apt nanostars displayed an increased absorption at 260 nm and a more negative surface charge than Au@Ag@-PEG nanostars due to the presence of the aptamer (Fig. 1F). Transmission electron microscopy (TEM) image showed that Au@Ag@PEG/Apt had an irregular sphere with an average diameter of 67.7 ± 5.1 nm (Fig. 1G). Moreover, Au@Ag@PEG/Apt showed a clear core–shell structure with the sharp tips of AuNS completely coated by the silver shell (Fig. 1H and S1†). The molar ratio of Au and Ag was 5.7 : 1 by the quantitative analysis *via* inductively coupled plasma atomic absorption spectrometer (ICP-AAS) measurements (Table S1†). As expected, Au@Ag@PEG/Apt exhibited good stability in complex biological environments or upon different treatments, with no significant changes in physicochemical properties, which was critical for biomedical applications (Fig. S3†).

Triggering of dormant photothermal and photoacoustic agent into active state for controllable thermoplasmonics

The optical, photothermal and photoacoustic responsiveness of the nanoagent toward overexpressed H_2O_2 [42] in the tumor microenvironment were then investigated by subjecting

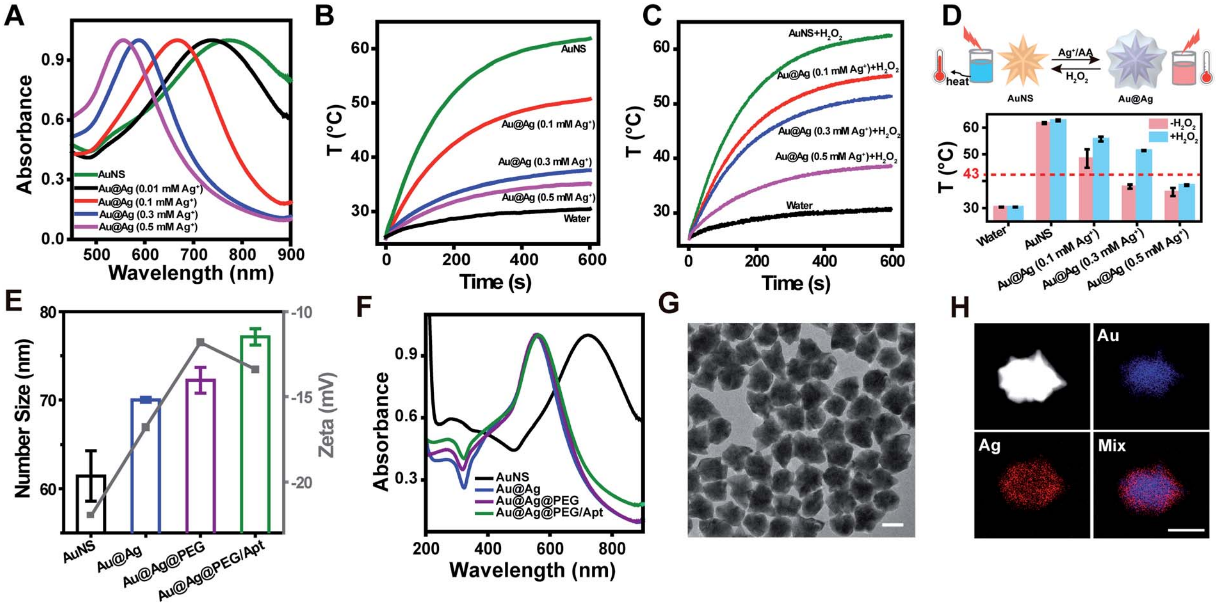

Fig. 1 Preparation and characterization of the tailored nanoarchitecture as a photoagent prodrug with fine-tuned plasmonic heating. (A) UV-vis absorption spectra of AuNS upon addition of different concentrations of silver ions to form Au@Ag nanostars. The spectra were normalized to unity. (B) Time-dependent temperature change curves of Au@Ag nanostars prepared with different concentrations of Ag^+ deposition upon exposure to a 808 nm NIR laser at a power density of 1 W cm^{-2}. (C) Revitalizing the photothermal capability of Au@Ag nanostars by 100 μM H_2O_2 etching of the coated Ag. The laser wavelength was 808 nm and the power density was 1 W cm^{-2}. (D) Temperature elevation of Au@Ag NS at $t = 600$ s in the absence (red) and presence (blue) of H_2O_2 according to the curves in (B) and (C) (down) and schematic illustration of the dormancy and activation process between AuNS and Au@Ag nanostars (top). Data are represented as mean ± SD ($n = 3$). (E and F) DLS analysis (E) and normalized absorbance spectra (F) of AuNS, Au@Ag, Au@Ag@PEG, and Au@Ag@PEG/Apt. Data are represented as mean ± SD ($n = 3$). (G and H) TEM image (G) and STEM-EDX element mapping (H) of Au@Ag@PEG/Apt. Scale bar, 50 nm.

Au@Ag@PEG/Apt to different concentrations of H_2O_2 (Fig. 2A). Following the confirmation of the dose-dependent effect of H_2O_2 on activating the photothermal performance of Au@Ag nanostars (Fig. S4†), we investigated the morphological dynamics of Au@Ag@PEG/Apt upon H_2O_2 stimulus (Fig. 2B). With increased H_2O_2 concentrations, the silver shell was

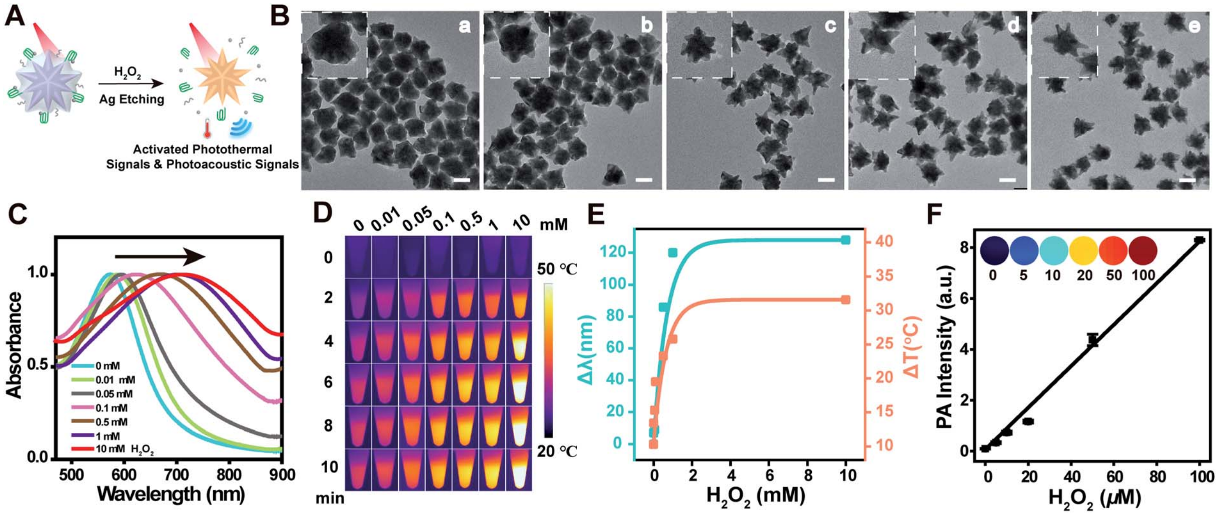

Fig. 2 Morphological and physicochemical dynamics of the photoagents upon H_2O_2 activation. (A) Schematic illustration of the H_2O_2-triggered photothermal effect and photoacoustic signal of Au@Ag@PEG/Apt. (B) Morphological dynamics of Au@Ag@PEG/Apt under H_2O_2 treatment. H_2O_2 concentration: (a) 0, (b) 0.1, (c) 0.5, (d) 1, and (e) 10 mM. The inset shows the magnified TEM images. (C and D) Normalized UV-vis absorption spectra (C) and IR thermal images (D) of the nanoprobe upon reacting with H_2O_2 at different concentrations. The laser wavelength is 808 nm with a power density of 1 W cm^{-2}. (E) Dependence of the red-shifted wavelength and elevated temperature on H_2O_2 concentration. (F) Enhanced PA signals of the nanoprobes at 795 nm in the presence of H_2O_2 (0, 5, 10, 20, 50, and 100 μM). The inset shows the PA images and the six colors represent different PA intensities. Scale bar, 50 nm. Data are represented as mean ± SD ($n = 3$).

gradually etched, accompanied with the exposure of the sharp tips of AuNS; moreover, the absorption spectrum red-shifted to the NIR region (Fig. 2C). These data provided the feasibility of Au@Ag@PEG/Apt for H_2O_2-activated PA imaging and PTT. It should be noted that the nanoprobe was also responsive to other types of reactive oxygen species (ROS) besides H_2O_2 (Fig. S5†). A comparison of the LSPR shift of Au@Ag@PEG/Apt toward different ROS indicated that the nanoprobe was also strongly reactive to $OH^\bullet$. Yet, there is a higher level and longer half-life of H_2O_2 than $OH^\bullet$ in live cells, especially in the tumor microenvironment.[46–48] Next, photothermal and photoacoustic images of the nanoprobes were recorded in the presence of various H_2O_2 concentrations upon laser irradiation. Time-dependent thermal images showed a significant temperature enhancement from 33.1 °C to 55 °C as the concentration of H_2O_2 increased (Fig. 2D and S6†). Notably, the photothermal conversion efficiency (η) of Au@Ag@PEG/Apt was calculated to be 49% after silver etching with H_2O_2 (Fig. S7†), which was higher than that of previous agents. Plots of the signal changes as a function of H_2O_2 concentration confirmed a high sensitivity of the nanoprobe (Fig. 2E). Similarly, due to the enhanced NIR absorption, PA images revealed more intense photoacoustic signals with elevated H_2O_2 levels, as well as a linear relationship (Fig. 2F). These data provide sensitive approaches to quantitatively and qualitatively sense H_2O_2 with the theranostic agents. The results demonstrate that Au@Ag@PEG/Apt has an *in situ* triggered and excellent photothermal effect and photoacoustic signal upon H_2O_2 activation, and acts as a promising candidate for precise tumor imaging and effective cancer treatment.

Fluorescence imaging of H_2O_2 dynamics in live cells

By modifying the aptamer with a fluorophore (TAMRA), Au@Ag@PEG/Apt-TAMRA was obtained as a fluorescence probe to follow H_2O_2 dynamics in cancer cells (Fig. S12A†). The nanoprobe targets cancer cells through specific binding between the aptamer (AS1411) and the overexpressed receptor (nucleolin) on the cell surface, and is internalized efficiently into the cancer cells. The fluorescence of TAMRA could be quenched by gold–silver nanostars due to energy transfer, whereas the signal would be recovered after the silver shell etching because of the fluorophore being away from the AuNS.

To verify the selective internalization of the activatable nanoprobes, cells with different expression of nucleolin were utilized. An obviously higher cellular uptake of the nanoprobes was observed in nucleolin-positive cells (MDA-MB-231 and 4T1 cells, breast cancer cells), but an extremely lower uptake by nucleolin-negative cells (HEK-293T, human embryonic kidney transformed cells) (Fig. S8†). The specific targeting was further demonstrated through a competitive inhibition assay using free AS1411 to block nucleolin. As shown in Fig. S9,† Au@Ag@PEG/Apt-treated cells had a stronger fluorescence signal than the cells pretreated with AS1411, confirming the specific targeting of the nanoprobes. In addition, the fluorescence intensities of the nanoprobes in cancer cells showed a gradual increase with extended incubation time (Fig. S8 and S10†). These data showed the specific and efficient internalization of the nanoprobes into cancer cells but not normal cells, showing great potential for precise theranostics.

Next, fluorescence activation of the nanoprobes by environmental signals was investigated. The study in aqueous solution confirmed that the fluorescence of the nanoprobes was strongly dependent on H_2O_2 levels, and increased dramatically with increased H_2O_2 concentration (Fig. S11†). To investigate the response of the nanoprobes toward H_2O_2 dynamics in cancer cells, ascorbic acid (AA, 2 mM) and antioxidant *N*-acetylcysteine (NAC, 10 mM) were used to treat the cells for H_2O_2 generation[49,50] and elimination,[51,52] respectively. Intracellular H_2O_2 levels upon different treatments were measured using the hydrogen peroxide assay kit in MDA-MB-231 cells and 4T1 cells (Fig. S12B and C†). The results showed that the H_2O_2 content in AA-treated cancer cells was remarkably higher than that in the control cells, and was significantly lower in the NAC-treated group and the nanoagent-treated group. In addition, the cells treated with both nanoprobes and AA had a low amount of H_2O_2, indicating the strong reactivity of nanoprobes with H_2O_2 for depletion. Correspondingly, flow cytometry (Fig. S12D and E†) and fluorescence confocal microscopy (Fig. S12F†) successively analyzed H_2O_2 dynamics in cancer cells. The brightest intracellular red fluorescence of TAMRA was observed for AA-treated cells, while the weakest fluorescence was observed for the cells treated with NAC. These results demonstrated that the nanoprobes could be effectively activated by the signal molecule, and were successively utilized for fluorescence imaging of H_2O_2 dynamics in cancer cells.

Targeted and activatable *in vitro* photothermal therapy with cancer cell specificity using the photoagent as prodrug

Based on the efficient tumor-specific internalization and H_2O_2 activated photothermal effect of the nanoagents, therapeutic efficacy of the phototheranostic agents at the cellular level was tested. 3-(4,5-Dimethylthialzol-2-yl)-2,5-diphenyltetrazolium bromide (MTT) assay (Fig. 3A) indicated that Au@Ag@PEG/Apt reduced cancer cell viability in a dose-dependent manner upon laser irradiation. Slight cytotoxicity was observed in the Au@Ag@PEG/Apt group without laser irradiation when the concentration increased to 80 μg mL^{-1}, which might be derived from the released Ag^+ upon H_2O_2 etching.[53] What's more, the relative cell viability was reduced to around 29.2% when challenged with 100 μg mL^{-1} Au@Ag@PEG/Apt plus laser irradiation. Such cytotoxicity was higher than that subjected to Au@Ag@PEG/Apt without laser irradiation or Au@Ag@PEG plus laser irradiation (Fig. S13†). In addition, there was no obvious cytotoxicity in normal cells in the presence or absence of laser irradiation due to the negligible uptake and dormant state of the nanoagents. Featuring targeted and *in situ* triggered photothermal responses, Au@Ag@PEG/Apt was thus a potential nanoagent for precise PTT toward cancer cells (Fig. 3B). Viability of cancer cells with different treatments was studied *via* fluorescence staining of live and dead cells with calcein-AM and propidium iodide (PI) (Fig. 3C). Almost all cancer cells incubated with Au@Ag@PEG/Apt died after 808 nm laser irradiation, while no significant damage appeared without irradiation.

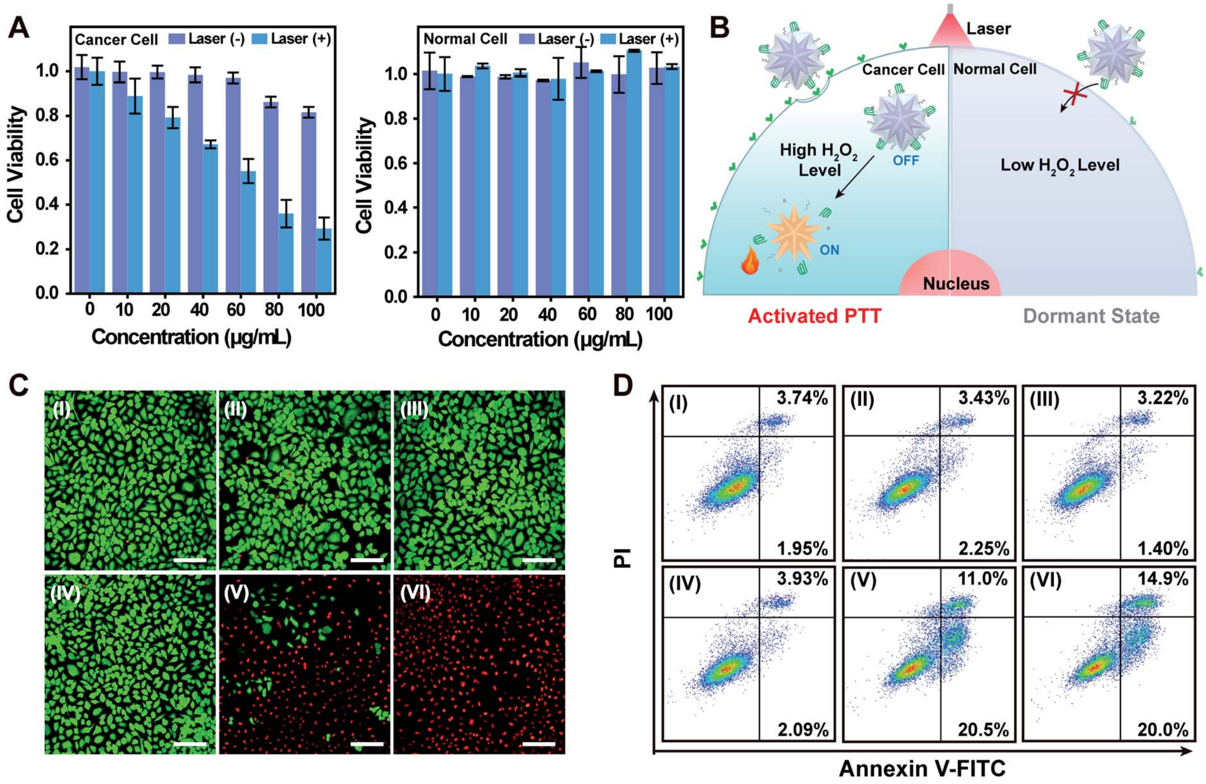

Fig. 3 Cancer cell targeted and activated *in vitro* photothermal therapy with the photoagent prodrug. (A) Viability of cancer cells (MDA-MB-231 cells, left) and normal cells (HEK-293T cells, right) incubated with nanoagents in the presence or absence of NIR laser irradiation. Data are represented as mean ± SD ($n = 5$). (B) Schematic illustration of the *in situ* reenergized dormant photothermal agent for precise cancer therapy using Au@Ag@PEG/Apt. (C and D) Fluorescence-based live/dead cell staining (C) and cell apoptosis (D) assays of MDA-MB-231 cells under different treatments: (I) PBS, (II) PBS plus laser irradiation, (III) Au@Ag@PEG, (IV) Au@Ag@PEG/Apt, (V) Au@Ag@PEG plus laser irradiation, and (VI) Au@Ag@PEG/Apt plus laser irradiation. The laser wavelength is 808 nm and the power density is 1 W cm^{-2}. Scale bar, 140 μm.

Due to the lack of an active targeting aptamer, Au@Ag@PEG induced less cell death than Au@Ag@PEG/Apt when both were subjected to laser irradiation. Consistent with the live and dead co-staining results, flow cytometric analysis (Fig. 3D and S14†) showed that phototherapy with the nanotherapeutics had the maximum apoptosis (34.9%, sum of annexinV-FITC$^+$/PI$^+$ and annexinV-FITC$^+$/PI$^-$). Taken together, NIR photo-ablation of cancer cells by Au@Ag@PEG/Apt enables great efficiency and selectivity.

Photoacoustic imaging of tumors and metastatic lymph nodes with *in situ* activated nanoagent

For further *in vivo* theranostic applications, pharmacokinetics and biodistribution of Au@Ag@PEG/Apt were first investigated. The half-life for distribution ($t_{1/2\alpha}$) and elimination ($t_{1/2\beta}$) was calculated to be 0.51 and 5.23 h (Fig. S15†), respectively, ensuring effective tumor accumulation of the nanoagents.[54] The biodistribution of the Au content in the main organs was measured using ICP-MS (Fig. S16†). The materials were mainly accumulated in the liver, a typically reticuloendothelial system organ, and tumors, which was attributed to the specific affinity between the AS1411 aptamer and receptor on the cancer cell surface. Such a selective accumulation at tumor sites is the most essential prerequisite for tumor-specific diagnosis and therapy.

To illustrate the *in vivo* photoacoustic response of the nanoprobes toward tumor signals, we intratumorally (i.t.) injected NAC and PBS separately into tumor-bearing mice, followed by i.t. injection of Au@Ag@PEG/Apt after 12 h (Fig. 4A). Time-dependent images showed a weaker PA signal for the mice treated with NAC compared to that of the control group due to the elimination of the endogenous H_2O_2 by NAC (Fig. 4B and C). The data implied the correlation of H_2O_2 levels in tumors to the PA intensity. For the mice intravenously (i.v.) injected with Au@Ag@PEG/Apt, the real-time photoacoustic imaging of tumors indicated that the signals gradually increased over time and reached the maximum at 24 h post injection (Fig. S17†).

Besides photoacoustic imaging of primary tumors, we challenged the nanoprobes with imaging of lymph node metastasis (Fig. 4D), as accurate detection of lymph node metastasis is of great significance to optimize therapeutic strategies and assess patient outcomes.[55] H&E and cytokeratin 8 (CK8) staining confirmed the successful invasion of tumor cells into the lymph nodes (Fig. S18†). After Au@Ag@PEG/Apt injection into the interstitial space of the legs, an obvious PA signal in the metastatic lymph nodes quickly emerged and gradually increased over time; while no detectable PA signal was observed in normal lymph nodes (Fig. 4E and F). The data indicated that Au@Ag@PEG/Apt could accurately detect lymph node metastasis.

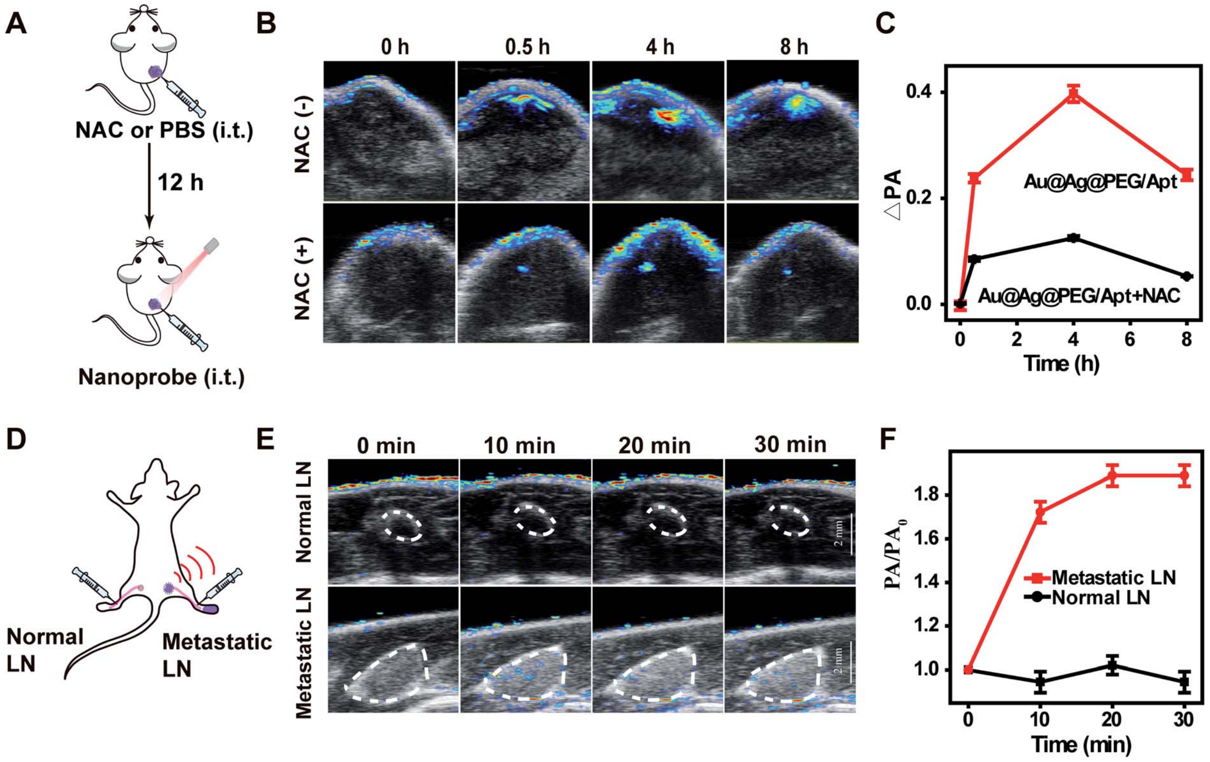

Fig. 4 Tumor microenvironment signal triggers photoacoustic imaging of tumors and metastatic lymph nodes with Au@Ag@PEG/Apt. (A) Experimental setup for photoacoustic imaging of tumors with H_2O_2 stimulus. NAC or PBS was first injected into the tumors, and then Au@Ag@PEG/Apt was i.t. injected after 12 h. (B and C) Time-dependent PA images (B) and corresponding PA intensity increment (C) at tumor sites. (D) Experimental setup for photoacoustic imaging of lymph node metastasis. Following the subcutaneous implantation of 4T1 breast tumor cells into the right hind footpad of mice, Au@Ag@PEG/Apt was injected into the interstitial space between the primary tumors and the metastatic lymph nodes. (E and F) Time-dependent PA images (E) and the corresponding relative intensities (F) of normal and metastatic lymph nodes. Data are represented as mean ± SD ($n = 3$).

Precise targeting and photothermal imaging of tumors for effective cancer phototherapy with high specificity

In vivo imaging and treatment of tumors with the theranostic photothermal agents were investigated in a subcutaneous tumor model. The temperature in the tumor area of the mice injected with Au@Ag@PEG/Apt showed a significant increase from 33.7 °C to 45.9 °C under laser irradiation (Fig. 5A and S19†). Temperature changes were dependent on the level of endogenous H_2O_2 (Fig. 5B and S20†), which was consistent with the fact that the agent was *in situ* activated by overexpressed H_2O_2 in the tumor microenvironment. These results demonstrate the effective activation of Au@Ag@PEG/Apt in tumors for photothermal imaging. To demonstrate the precise theranostics with the agents, the activatable nanoprobe (Au@Ag@PEG/Apt) and an always-on nanoprobe (AuNS) were respectively injected into tumors or muscles for comparison. For the Au@Ag@PEG/Apt group, bright images were observed specifically in the tumor area due to the marked difference in H_2O_2 levels between the tumor and muscle. However, for the AuNS group, the muscle areas showed distinct background signals, and a smaller difference in signal intensity was observed between the tumor and muscle compared with that of the Au@Ag@PEG/Apt group (Fig. 5C and D). Thus, the *in situ* activatable nanoprobe achieved specific infrared thermal imaging of tumor tissues, which is beneficial to tumor-specific PTT that can avoid side effects on normal tissues.

To evaluate the antitumor effect of Au@Ag@PEG/Apt *in vivo*, 4T1 tumor-bearing mice were randomly divided into five groups with different treatments (Fig. 5E). The most significant tumor growth suppression was observed in the Au@Ag@PEG/Apt-treated group with laser irradiation, which was ascribed to the active targeting of the AS1411 aptamer and effectively activated-PTT (Fig. 5F and S21†). Tumor cell death was evaluated by hematoxylin and eosin (H&E) staining and terminal deoxynucleotidyl transferase dUTP nick end labeling (TUNEL) staining of the tumor tissues. In the H&E staining assay, severe membrane structural destruction and disintegrated nuclei were observed in group IV and group V, demonstrating obvious cell apoptosis and/or necrosis of cancer cells. In addition, the TUNEL assay showed that strong green fluorescence was observed in the Au@Ag@PEG + laser group and Au@Ag@PEG/Apt + laser group, indicating serious DNA damage and cell apoptosis, which was consistent with the results of H&E assay (Fig. 5G). The data further proved the excellent antitumor effect of the activatable photothermal agents. We also investigated whether there were possible potential side effects. During *in vivo* treatments, a negligible change in mice body weight was observed in all groups (Fig. S22†). In addition, blood

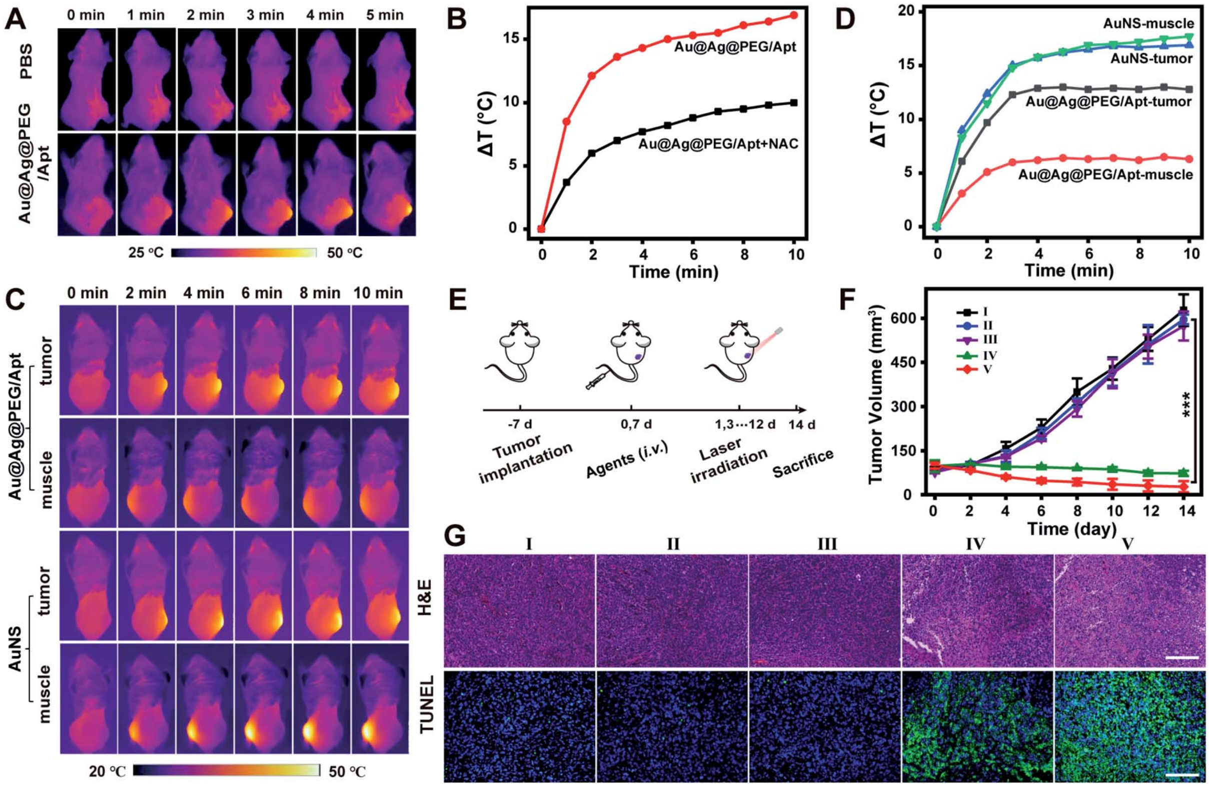

Fig. 5 *In situ* activation of photothermal agents enables precise tumor imaging and specific cancer treatment in a subcutaneous tumor model. (A) Infrared thermal images of 4T1-bearing mice i.v. injected with PBS or Au@Ag@PEG/Apt under laser irradiation. (B) Difference in temperature increase of 4T1 tumor-bearing mice after i.t. injection of Au@Ag@PEG/Apt with or without NAC pre-injection indicates the activation of photothermal agents *in situ* by overexpressed H_2O_2. (C) Infrared thermal images of tumors and muscles after separate intratumor and intramuscular injection with Au@Ag@PEG/Apt or AuNS. (D) Comparison of the *in situ* activated and the "always on" nanoagents on the specificity of tumor thermal imaging from (C). (E) Schematic illustration of the *in vivo* therapeutic process. (F) Tumor volume of mice upon different treatments. Statistical significance was calculated *via* one-way ANOVA with the Bonferroni multiple comparison post-test (***$P < 0.001$); data are represented as mean ± SD ($n = 4$). (G) Representative images of H&E and TUNEL stained tumor slices at day 2 post laser irradiation. (I) PBS + laser, (II) Au@Ag@PEG, (III) Au@Ag@PEG/Apt, (IV) Au@Ag@PEG + laser, and (V) Au@Ag@PEG/Apt + laser. Laser wavelength, 808 nm; power density, 1 W cm^{-2}. Scale bar, 100 μm.

biochemistry analysis showed that there was no obvious difference in measured markers, revealing no toxicity of the nanoagents in mice at the given dose (Fig. S23†). Also, H&E staining of major organs at the 14th day after the respective treatment indicated no apparent pathological damage (Fig. S24†). These results validated that Au@Ag@PEG/Apt possessed good biosafety for *in vivo* applications.

Conclusion

In summary, we have described a tumor microenvironment activated prodrug for precision cancer treatment and diagnosis by controllable thermoplasmonics. In response to signal molecules, photothermal and photoacoustic signals are *in situ* triggered through revitalization of dormant plasmonic nanoparticles, enabling precise imaging and specific ablation of cancer cells. This approach is applicable as plasmonic nanoparticles are readily engineered for tunable and activated LSPR and light-to-heat conversion. As such, the method allows sensitive photoacoustic, photothermal and fluorescence imaging of overexpressed H_2O_2 dynamics *in vitro* and *in vivo*. Importantly, *in situ* triggering of the photothermal and photoacoustic agent to the active state enables real-time imaging of tumors and lymph node metastasis with high specificity, as well as precise PTT for effective tumor ablation. Overall, our study provides an activatable photoagent with good biocompatibility, high specificity and high efficacy for precision therapeutics and theranostics.

This solution to the nonspecificity problem opens a facile and practical access to precision diagnosis and targeted therapy, with implications for translation. As far as we know, activatable thermoplasmonics for cancer diagnosis or nanomedicine remain exclusive. As plasmonic nanoparticles are exquisitely sensitive to size, shape and composition of the structure,[55] this method provides a big opportunity to rationally design diverse plasmonic architectures as activatable theranostic probes. In addition, the revitalization method may be applicable to more nanosources of heat[56,57] besides plasmonic nanoparticles for developing precision medicine.[19–21] Considering the emerging research activities of thermoplasmonics in different fields of science from biomedicine to imaging and catalysis,[58] such fine-tuned plasmonic heating may foster a variety of applications.

Ethical statement

All animal procedures were in accordance with the National Institute of Health Guide for the Care and Use of Laboratory Animals and approved by Use Committee of the Animal Experiment Center/Animal Biosafety Level-III Laboratory of Wuhan University (license number: WP2020-08047).

Author contributions

X. Liu and Y. Liu conceived the study and designed the experiment. Y. Liu and F. Mo performed the main experiments and analyzed the data. J. Hu, Q. Jiang and X. Wang assisted with *in vivo* experiments. Z. Zou participated in the manuscript preparation. D. W. Pang and X. Z. Zhang provided technical support. All authors participated in the writing of the manuscript.

Conflicts of interest

There are no conflicts to declare.

Acknowledgements

This work was supported by the National Natural Science Foundation of China (51833007) and the Fundamental Research Funds for the Central Universities (No. 2042018kf1006).

Notes and references

1 Y. Liu, J. Wang, Q. Xiong, D. Hornburg, W. Tao and O. C. Farokhzad, *Acc. Chem. Res.*, 2021, **54**, 291–301.
2 E. K. Lim, T. Kim, S. Paik, S. Haam, Y. M. Huh and K. Lee, *Chem. Rev.*, 2015, **115**, 327–394.
3 K. Heinzmann, L. M. Carter, J. S. Lewis and E. O. Aboagye, *Nat. Biomed. Eng.*, 2017, **1**, 697–713.
4 L. Ricciardi, L. Sancey, G. Palermo, R. Termine, A. De Luca, E. I. Szerb, I. Aiello, M. Ghedini, G. Strangi and M. La Deda, *Nanoscale*, 2017, **9**, 19279–19289.
5 J. Jia, G. Liu, W. Xu, X. Tian, S. Li, F. Han, Y. Feng, X. Dong and H. Chen, *Angew. Chem., Int. Ed.*, 2020, **59**, 14443–14448.
6 X. Li, J. F. Lovell, J. Yoon and X. Chen, *Nat. Rev. Clin. Oncol.*, 2020, **17**, 657–674.
7 X. Zhao, J. Liu, J. Fan, H. Chao and X. Peng, *Chem. Soc. Rev.*, 2021, **50**, 4185–4219.
8 X. Li, S. Lee and J. Yoon, *Chem. Soc. Rev.*, 2018, **47**, 1174–1188.
9 A. S. Schwartz-Duval, C. J. Konopka, P. Moitra, A. E. Daza, I. Srivastava, E. V. Johnson, T. L. Kampert, S. Fayn, A. Haran, L. W. Dobrucki and D. Pan, *Nat. Commun.*, 2020, **11**, 4530.
10 G. Baffou and R. Quidant, *Laser Photonics Rev.*, 2013, **7**, 171–187.
11 S. He, Y. Jiang, J. Li and K. Pu, *Angew. Chem., Int. Ed.*, 2020, **59**, 10633–10638.
12 Y. Wang, N. Gong, Y. Li, Q. Lu, X. Wang and J. Li, *J. Am. Chem. Soc.*, 2020, **142**, 1735–1739.
13 H. Huang, S. Banerjee, K. Qiu, P. Zhang, O. Blacque, T. Malcomson, M. J. Paterson, G. J. Clarkson, M. Staniforth, V. G. Stavros, G. Gasser, H. Chao and P. J. Sadler, *Nat. Chem.*, 2019, **11**, 1041–1048.
14 M. Pan, Q. Jiang, J. Sun, Z. Xu, Y. Zhou, L. Zhang and X. Liu, *Angew. Chem., Int. Ed.*, 2020, **59**, 1897–1905.
15 C. Liang, X. Zhang, M. Yang, W. Wang, P. Chen and X. Dong, *ACS Mater. Lett.*, 2020, **2**, 1268–1286.
16 Q. Jiang, M. Pan, J. Hu, J. Sun, L. Fan, Z. Zou, J. Wei, X. Yang and X. Liu, *Chem. Sci.*, 2021, **12**, 148–157.
17 S. Nomura, Y. Morimoto, H. Tsujimoto, M. Arake, M. Harada, D. Saitoh, I. Hara, E. Ozeki, A. Satoh, E. Takayama, K. Hase, Y. Kishi and H. Ueno, *Sci. Rep.*, 2020, **10**, 9765.
18 G. Baffou, *Photoniques*, 2018, 42–47.
19 R. van der Meel, E. Sulheim, Y. Shi, F. Kiessling, M. W. J. ulder and T. Lammers, *Nat. Nanotechnol.*, 2019, **14**, 1007–1017.
20 M. J. Mitchell, M. M. Billingsley, R. M. Haley, M. E. Wechsler, N. A. Peppas and R. Langer, *Nat. Rev. Drug Discovery*, 2020, 1–24.
21 M. T. Manzari, Y. Shamay, H. Kiguchi, N. Rosen, M. Scaltriti and D. A. Heller, *Nat. Rev. Mater.*, 2021, 1–20.
22 J. Li and K. Pu, *Acc. Chem. Res.*, 2020, **53**, 752–762.
23 L. Wu, Y. Sun, K. Sugimoto, Z. Luo, Y. Ishigaki, K. Pu, T. Suzuki, H. Y. Chen and D. Ye, *J. Am. Chem. Soc.*, 2018, **140**, 16340–16352.
24 M. H. Lee, A. Sharma, M. J. Chang, J. Lee, S. Son, J. L. Sessler, C. Kang and J. S. Kim, *Chem. Soc. Rev.*, 2018, **47**, 28–52.
25 B. M. Luby, C. D. Walsh and G. Zhang, *Angew. Chem., Int. Ed.*, 2019, **58**, 2558–2569.
26 Y. Jiang, J. Huang, C. Xu and K. Pu, *Nat. Commun.*, 2021, **12**, 742.
27 Y. Zhang, C. Xu, X. Yang and K. Pu, *Adv. Mater.*, 2020, **32**, 2002661.
28 J. Li, D. Cui, Y. Jiang, J. Huang, P. Cheng and K. Pu, *Adv. Mater.*, 2019, **31**, 1905091.
29 L. An, X. Wang, X. Rui, J. Lin, H. Yang, Q. Tian, C. Tao and S. Yang, *Angew. Chem., Int. Ed.*, 2018, **57**, 15782–15786.
30 Q. Chen, C. Liang, X. Sun, J. Chen, Z. Yang, H. Zhao, L. Feng and Z. Liu, *Proc. Natl. Acad. Sci. U. S. A.*, 2017, **114**, 5343–5348.
31 B. Shi, Q. Yan, J. Tang, K. Xin, J. Zhang, Y. Zhu, G. Xu, R. Wang, J. Chen, W. Gao, T. Zhu, J. Shi, C. Fan, C. Zhao and H. Tian, *Nano Lett.*, 2018, **18**, 6411–6416.
32 H. Wang, J. Chang, M. Shi, W. Pan, N. Li and B. Tang, *Angew. Chem., Int. Ed.*, 2019, **58**, 1057–1061.
33 P. Chen, Y. Ma, Z. Zheng, C. Wu, Y. Wang and G. Liang, *Nat. Commun.*, 2019, **10**, 1192.
34 Y. Lyu, C. Xie, S. A. Chechetka, E. Miyako and K. Pu, *J. Am. Chem. Soc.*, 2016, **138**, 9049–9052.
35 E. Prodan, C. Radloff, N. J. Halas and P. Nordlander, *Science*, 2003, **302**, 419–422.

36 S. Link, Z. L. Wang and M. A. El-Sayed, *J. Phys. Chem. B*, 1999, **103**, 3529–3533.

37 Y. C. Tsao, S. Rej, C. Y. Chiu and M. H. Huang, *J. Am. Chem. Soc.*, 2014, **136**, 396–404.

38 Y. Liu, M. Pan, W. Wang, Q. Jiang, F. Wang, D. W. Pang and X. Liu, *Anal. Chem.*, 2019, **91**, 2086–2092.

39 H. Chen, L. Shao, T. Ming, Z. Sun, C. Zhao, B. Yang and J. Wang, *Small*, 2010, **6**, 2272–2280.

40 D. Yoo, H. Jeong, S. H. Noh, J. H. Lee and J. Cheon, *Angew. Chem., Int. Ed.*, 2013, **52**, 13047–13051.

41 T. P. Szatrowski and C. F. Nathan, *Cancer Res.*, 1991, **51**, 794–798.

42 H. Zhu, J. Li, X. Qi, P. Chen and K. Pu, *Nano Lett.*, 2018, **18**, 586–594.

43 H. Otsuka, Y. Nagasaki and K. Kataoka, *Adv. Drug Delivery Rev.*, 2003, **55**, 403–419.

44 H. Yuan, A. M. Fales and T. Vo-Dinh, *J. Am. Chem. Soc.*, 2012, **134**, 11358–11361.

45 O. C. Farokhzad, J. M. Karp and R. Langer, *Expert Opin. Drug Delivery*, 2006, **3**, 311–324.

46 H. Sies and D. P. Jones, *Nat. Rev. Mol. Cell Biol.*, 2020, **21**, 363–383.

47 B. Yang, Y. Chen and J. Shi, *Chem. Rev.*, 2019, **119**, 4881–4985.

48 S. Parvez, M. J. C. Long, J. R. Poganik and Y. Aye, *Chem. Rev.*, 2018, **118**, 8798–8888.

49 Q. Chen, M. G. Espey, A. Y. Sun, J. H. Lee, M. C. Krishna, E. Shacter, P. L. Choyke, C. Pooput, K. L. Kirk, G. R. Buettner and M. Levine, *Proc. Natl. Acad. Sci. U. S. A.*, 2007, **104**, 8749–8754.

50 Q. Chen, M. G. Espey, M. C. Krishna, J. B. Mitchell, C. P. Corpe, G. R. Buettner, E. Shacter and M. Levine, *Proc. Natl. Acad. Sci. U. S. A.*, 2005, **102**, 13604–13609.

51 A. Gillissen and D. Nowak, *Respir. Med.*, 1998, **92**, 609–623.

52 M. Kasielski and D. Nowak, *Respir. Med.*, 2001, **95**, 448–456.

53 S. Kim, J. E. Choi, J. Choi, K. H. Chung, K. Park, J. Yi and D. Y. Ryu, *Toxicol. In Vitro*, 2009, **23**, 1076–1084.

54 C. Bi, J. Chen, Y. Chen, Y. Song, A. Li, S. Li, Z. Mao, C. Gao, D. Wang, H. Möhwald and H. Xia, *Chem. Mater.*, 2018, **30**, 2709–2718.

55 C. L. Chaffer and R. A. Weinberg, *Science*, 2011, **331**, 1559–1564.

56 G. Baffou and R. Quidant, *Chem. Soc. Rev.*, 2014, **43**, 3898–3907.

57 L. Jauffred, A. Samadi, H. Klingberg, P. M. Bendix and L. B. Odd-ershede, *Chem. Rev.*, 2019, **119**, 8087–8130.

58 G. Baffou, F. Cichos and R. Quidant, *Nat. Mater.*, 2020, **19**, 946–958.